-RESEARCH PAPER-

International Journal of Mining and Geo-Engineering

IJMGE

IJMGE 60-3 (2026) 267-276

DOI: 10.22059/ijmge.2026.406956.595337

Airborne time-domain electromagnetic investigation of the Granisle polymetallic deposit: qualitative interpretation and rapid conductivity-depth imaging

Mohammad Saleh Ahmadi [a], Ali Jafarabadi [a], Maysam Abedi [a,*], and Ali Moradzadeh [a]

[a] *School of Mining Engineering, College of Engineering, University of Tehran, Tehran, Iran*

Article History:

Received: 24 November 2025.
Revised: 25 December 2025.
Accepted: 13 May 2026.

ABSTRACT

Airborne time-domain electromagnetic (ATEM) surveys have emerged as one of the most effective tools for detecting conductive structures and concealed mineral targets, achieving remarkable accuracy and efficiency in recent years. In this study, airborne electromagnetic data from the QUEST-West project were utilized to reconstruct the three-dimensional geometry of alteration and mineralization zones within the Granisle porphyry Cu–Au deposit in the Babine district of British Columbia. Qualitative analysis of off-time channels and the Late Time Decay Constant (τ) map revealed three prominent conductive zones with a northeast–southwest trend. In addition, conductivity-depth imaging (CDI), implemented via a fast approximate transform, was applied to generate independent depth sections for each flight line, which were subsequently merged through multidimensional interpolation into a quasi–three-dimensional conductivity model. The CDI results indicate the presence of a focused conductive body with a shallow top (on the order of tens of meters below surface) and a significant vertical extent, spatially coincident with the historic open pit at the Granisle deposit—a geometry consistent with the known distribution of mineralized zones and vein networks at Granisle. By circumventing computationally intensive inversion procedures, this approach provides a stable and geologically coherent first-order image of subsurface conductivity and can serve as a reference model for quantitative inversion, drill targeting, and exploration decision-making in the historically mined Granisle porphyry deposit.

Keywords: *Airborne time-domain electromagnetics, Conductivity-depth imaging, Porphyry mineralization, Granisle deposit, Pseudo-3D conductivity model*

1. Introduction

The Airborne electromagnetic methods are widely employed for mineral prospecting, oil and gas resource investigation, groundwater exploration, and major engineering survey applications, particularly in regions with rugged topography—such as mountainous terrains, wetlands, and other areas with complex relief—where ground-based acquisition is difficult [1, 2]. Airborne methods offer advantages including high efficiency, relatively lower cost, and reduced sensitivity to surface and topographic conditions [3]. Based on the transmitter current waveform (harmonic or pulse), AEM methods are classified into frequency- and time-domain systems [4]. Time-domain AEM systems are further subdivided according to their mobile platform into fixed-wing and helicopter configurations. Historically, time-domain AEM systems have been considered to provide greater exploration depth but somewhat lower near-surface resolution compared to frequency-domain systems. However, significant technological advances within the past decade have enhanced the near-surface resolving capability of time-domain AEM systems to levels comparable with frequency-domain systems [5, 6].

In Iran, airborne electromagnetic (AEM) surveys have also exhibited a growing trend since the 1990s. A prominent example is the helicopter-borne HMER survey conducted in 1992 by Geonex Aerodat in Kerman Province, covering approximately 7,000 square kilometers with the objective of porphyry copper exploration, which led to the identification of key conductivity anomalies [7]. During the 2000s to 2010s, the application of HEM and HTEM systems expanded for deeper subsurface investigations and high-resolution mapping. Notable among these is the DIGHEM survey in 2011 in the Kalat-e-Reshm area of Semnan Province, aimed at constructing three-dimensional resistivity models in volcanic terrains [8]. In subsequent years, these datasets underwent reanalysis employing advanced processing techniques, particularly between 2018 and 2019, resulting in improved structural resolution and more precise identification of mineralization targets [9, 10]. This evolutionary trajectory clearly underscores the increasing prominence and effective role of electromagnetic methods in enhancing the efficiency of mineral resource exploration in Iran.

Electromagnetic methods operate by inducing electromagnetic fields and measuring the secondary responses generated by conductive or resistive subsurface zones, thereby enabling detection of spatial variations in bulk conductivity [11]. This capability renders EM techniques essential for mineral exploration, since strong contrasts in electrical resistivity—often spanning several orders of magnitude—commonly exist between conductive ore bodies such as sulfide deposits and their generally resistive host rocks [12].

By quantifying these secondary responses, EM methods can effectively identify and delineate mineralized zones, clay-rich or fluid-rich alteration halos, and geological structures such as faults that act as conduits or traps for conductive materials. This high sensitivity to conductivity anomalies enables non-invasive imaging of the subsurface

* Corresponding author. *E-mail address:* maysamabedi@ut.ac.ir (M. Abedi).

at high resolution, leading to more accurate drill targeting and reduced exploration risk [13].

Interpreting time-domain AEM data typically requires computationally expensive inversion to estimate subsurface resistivity distributions [14]. A standard inversion scheme incorporates formulation of an objective function, selection of an optimization strategy, and iterative computation of the electromagnetic forward response, often requiring hundreds of model evaluations per station [5]. To address this challenge, conductivity-depth imaging (CDI) methods provide a fast, stable, and preliminary depiction of subsurface conductivity without resorting to iterative inversion [15, 16]. CDI relies on deterministic transforms that map each EM decay channels to an apparent conductivity and corresponding depth of investigation using analytical half-space formulations [17]. By bypassing the sensitivity matrix and optimization loops, CDI can generate conductivity-depth sections within minutes, forming a critical bridge between raw data visualization and full quantitative inversion.

Numerous studies have demonstrated the effectiveness of conductivity-depth imaging in interpreting electromagnetic data and identifying concealed mineral targets while assessing subsurface conductivity architecture. For example, Huang and Rudd (2008) presented an enhanced CDI framework based on a pseudolayer half-space model for helicopter TEM data, significantly reducing ambiguity in depth and conductivity estimation and enabling higher-fidelity imaging of conductive ore bodies and geological structures in exploration environments [18]. Likewise, Liang et al. (2021) applied CDI to AeroTEM-IV time-domain airborne EM data in the Baishiquan–Hongliujing area of China, resolving low-resistivity anomalies associated with ferromagnesian–ultramafic rocks and alteration zones—results that ultimately led to the discovery of a previously unknown gold deposit with an estimated potential exceeding 10 tonnes [19]. In addition, Stolz et al. (2022) used CDI to interpret EM data from the Gergarub belt in Namibia, accurately delineating the lateral extent of a high-conductivity, subhorizontal Pb–Zn–Ag VMS sheet [20]. Collectively, these findings demonstrate the established utility of CDI for extracting structural information and identifying concealed mineralization from EM data—capabilities that are especially valuable in large, complex systems such as porphyry Cu deposits, where conductivity patterns closely reflect alteration processes and intrusive architectures.

Porphyry deposits represent the world's most significant sources of copper and molybdenum and constitute major resources of gold, silver, and tin. They supply approximately 50–60 percent of global copper and over 95 percent of molybdenum production [21]. Porphyry deposits form through hydrothermal alteration and mineralization associated with shallow porphyritic intrusions, predominantly within subduction-related magmatic arcs [22]. The evolutionary nature of porphyry systems concentrates mineral assemblages with diverse geophysical properties near the Earth's surface. A fundamental principle is that porphyry Cu mineralization is spatially zoned [23, 24], generating predictable electrical patterns. Iron and copper sulfides—including pyrite, chalcopyrite, chalcocite, and bornite—are widely distributed across the alteration and mineralized zones [22] and typically exhibit moderate to low resistivity [11], making them detectable and distinguishable in EM surveys [9, 25].

Among major copper-producing countries, Canada holds a prominent position and has consistently ranked among the world's top ten producers over the past decade. Geologically, Canada is one of the oldest continental regions, with more than half of its landmass composed of Precambrian rocks that have been exposed above sea level since early Paleozoic time [26]. Most Canadian copper production is derived from porphyry deposits within the Canadian Cordillera [27]. Among these, the Babine district is one of the most important and has a long mining history [21].

Early exploration in this district led to the discovery of the Granisle, Bell, and Morrison deposits. Granisle was mined as an open pit from 1966 until operations ceased in 1982 due to declining copper prices and unfavorable economic conditions [28]. In 2008, the QUEST-West project was launched to re-evaluate historical datasets and assess regional potential beneath glacial cover of variable thickness. High-resolution magnetic and electromagnetic surveys were acquired over six deposits, including Granisle [29].

Despite the availability of high-resolution airborne EM data from QUEST-West, the three-dimensional geometry of alteration zones at the Granisle deposit—particularly along the mineralized trend and at depth—remains insufficiently constrained. This study employs electromagnetic processing through two primary stages: (1) qualitative interpretation of off-time channels and Late Time Decay Constant (τ), and (2) CDI processing to estimate the subsurface conductivity distribution.

The objective is to provide a rapid, stable, and geologically reliable image of the Granisle subsurface. This workflow enables efficient reconstruction of the spatial architecture of alteration and conductive mineralized zones while preserving the relative depth positioning of anomalies with respect to local topography, particularly in areas associated with the phyllic zone. The principal advantage of this method compared to full inversion is the substantial reduction in computational time while producing a dependable initial model that can support subsequent quantitative analysis, drill targeting, and broader exploration decision-making.

2. Geological setting of the study area

The Babine district, located in central British Columbia within the Stikinia terrane, is one of the best-known Eocene magmatic–mineralized belts in northwestern Canada. The district extends along a northwest–southeast trend and is structurally controlled by dextral strike-slip faults that have accommodated prolonged deformation and magmatism from the mid-Cretaceous through the Eocene [30]. The regional geology comprises volcanic–sedimentary sequences of the Asitka, Takla and Hazelton groups, together with numerous intermediate to felsic intrusive bodies that record the evolution of volcanic-arc magmatism [31].

Eocene magmatism, coeval with transgressional and extensional fault activity, created favorable conditions for the concentration of calc-alkaline magmas and the development of associated hydrothermal systems that define the tectonomagmatic framework of porphyry systems in the Babine district. Within this framework, several porphyry systems developed, of which the Granisle copper-gold porphyry deposit is one of the most representative.

The Granisle porphyry Cu–Au deposit, situated on McDonald Island in Babine Lake in central British Columbia (Figure 1), is the southernmost of the three major porphyry systems in the Babine district [28]. Similar to the Bell and Morrison deposits, Granisle is genetically associated with Eocene intrusions of the Babine magmatic suite—particularly biotite–feldspar porphyry (BFP) and quartz diorite microporphyry emplaced into lower Jurassic volcanic–sedimentary rocks of the Hazelton Group [32]. These intrusions occupy north–northwest-trending faults associated with the Morrison graben, formed during a Late Cretaceous to early Tertiary extensional regime.

Two principal intrusive phases are recognized at Granisle: an early elliptical quartz diorite microporphyry with a northeast–southwest trend, and later crosscutting biotite–feldspar porphyry dikes, which locally exceed 200 m in thickness. BFP rocks exhibit a dense porphyritic texture with euhedral phenocrysts of plagioclase and biotite set in a fine-grained quartz–feldspar groundmass. K–Ar dating of biotite from both mineralized and barren rocks yields an average age of 51 ± 2 Ma, consistent with the timing of Eocene magmatism across the Babine porphyry systems [28]. Hydrothermal alteration at Granisle displays the characteristic concentric zoning typical of calc-alkaline porphyry systems. The central potassic zone—dominated by biotite, quartz, and magnetite—grades outward into a suite of carbonate–sericite–quartz–pyrite assemblages. The potassic core is spatially coincident with the main mineralized zone, where hydrothermal biotite and disseminated magnetite are widely developed within both BFP and volcanic host rocks. Outward from the core, pervasive sericitization and pyritization define a well-developed phyllic halo. Weak propylitic alteration,

characterized by chlorite, epidote, and carbonate, occurs along the margins of the system [32]. Copper mineralization is primarily disseminated and vein-hosted chalcopyrite and bornite within the potassic and inner phyllic zones, locally accompanied by minor molybdenite. Pyrite and marcasite are abundant in peripheral zones, comprising up to 5 percent of the rock volume. Compared to the Bell deposit, Granisle exposes a deeper erosional level of the Babine porphyry magmatic–hydrothermal system, revealing its root-zone architecture [28].

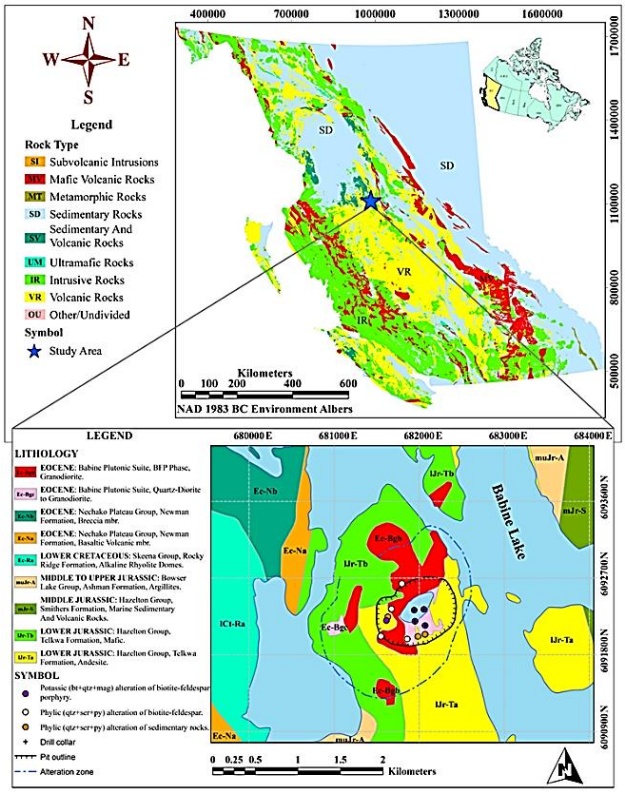

Figure 1. Regional geological map of British Columbia, Canada, showing the location of the Granisle polymetallic deposit (modified from [38]), together with the detailed geological map of the deposit area (modified from [32]).

3. Data and methods

3.1. Airborne time-domain electromagnetic data

The airborne geophysical dataset used in this study was acquired during a helicopter-borne electromagnetic and magnetic survey conducted as part of the Quest West Project in central British Columbia. The survey covered several sectors of the Babine district, including the Granisle deposit. Data acquisition took place from July 29 to October 23, 2008, yielding over 13,000 km of flight lines. In addition to the main traverse lines, multiple infill areas—including the Granisle deposit—were flown with a nominal line spacing of 200 m to increase data quality and spatial resolution over mineralized zones. Figure 2 shows the topography of the Granisle area along with airborne flight lines and the mineral pit boundary, delineating the spatial framework of the geophysical dataset.

The electromagnetic data were collected using an AeroTEM III time-domain system which employs a triangular pulse shape excitation waveform at a base frequency of 90 Hz and records full-waveform X- and Z-component responses at high sampling rates (Figure 3). Following initial sampling, the data were processed to a 10 Hz sample rate and organized into 33 stacked and binned channels comprising on-time and, particularly, off-time channels used for conductivity-depth imaging. The EM receiver was flown at a nominal altitude of 30 m, and flight positioning was maintained with real-time differential GPS to ensure reliable coordinates and elevations for accurate data processing. Flight speed was adjusted according to terrain to keep the system response within optimal operating range. High elevation checks and routine quality-control procedures were conducted to maintain data integrity.

Raw data underwent standard processing, including pre-filtering, stacking, binning, noise reduction via stacking processes, and leveling, and were then used to generate final products such as off-time channels and the Late Time Decay Constant (τ) [29]. Maps of four representative off-time channels selected from the 17 acquired channels, depicting variations in the secondary magnetic field, are shown in Figure 4, and the Late Time Decay Constant (τ) map is presented in Figure 5. A mineralization zone, with the Granisle deposit at its center, is outlined in Figures 4 and 5. This area was selected for focused subsurface analysis, and conductivity-depth imaging (CDI) was applied exclusively to the airborne data within this region to minimize the influence of large surrounding anomalies and more effectively resolve the deposit's subsurface structure.

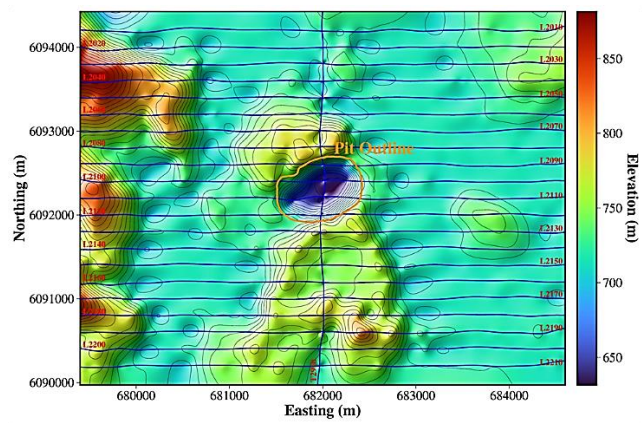

Figure 2. Topographic map of the study area showing the airborne geophysical survey flight lines and the outline of the mine pit.

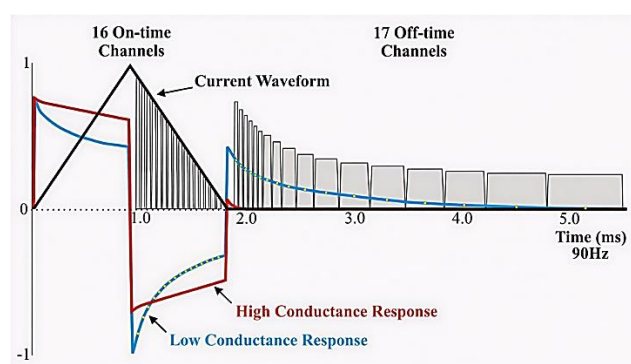

Figure 3. Schematic representation of curves for current wave form generated in the transmitter and inductive EM response obtained in the receiver [29].

3.2. Physical properties

Understanding resistivity behavior across lithological units is essential for credible interpretation of electromagnetic data. Examination of the Granisle deposit samples (Table 1) reveals that resistivity variations are closely related to lithology and alteration intensity. Potassic-altered intrusive rocks—particularly biotite–feldspar porphyry and quartz–diorite microporphyry—display the highest resistivity. These elevated values reflect relatively fresh textures, limited microfracturing, and the absence of conductive phases. Weakly altered granite also exhibits high resistivity (approximately 4,400 Ωm), behaving as a highly resistive electrical medium. In contrast, phyllic

alteration and quartz–sericite–carbonate–pyrite assemblages cause a pronounced reduction in resistivity, producing a range of approximately 200 to 2,073 Ωm. The presence of pyrite and the development of conductive fluid pathways in these zones constitute the principal cause of resistivity decline. Weakly altered extrusive biotite–feldspar porphyries exhibit the lowest resistivity among the samples (approximately 65 to 96 Ωm), likely attributable to surface weathering or elevated sulfide content. In andesitic tuffs affected by phyllic alteration, resistivity falls within an intermediate range (roughly 560 to 2,073 Ωm), indicating a reduced degree of conductive mineralization relative to phyllic-altered intrusive units.

3.3. Conductivity-depth imaging algorithm

Conductivity-depth imaging (CDI) over the region shown in Figure 5 was performed using the fast approximate transform introduced by Macnae et al. (1991) and later refined by Macnae et al. (1998) [15, 17]. This approach directly converts airborne time-domain electromagnetic (ATEM) data into a pseudo-layered conductivity–depth model without invoking conventional layered-earth inversion. The CDI methodology involves a series of well-defined, sequential processing steps designed to ensure transparency and reproducibility. Key parameters used in the implementation, including those derived from input data and algorithm settings, are summarized in Table 2. These parameters were selected based on standard implementations of the Macnae method and tuned for the AeroTEM III data characteristics to achieve stable imaging consistent with known geology. Sensitivity tests confirmed that variations in smoothing factor and depth resolution did not significantly alter the overall conductive body geometry.

The CDI algorithm proceeds through the following steps:

a) Data Transformation to Step-Response Waveform: The measured data (dB/dt or B-field) are transformed into an equivalent step-response waveform R(t), representing the subsurface impulse response:

$$R(t) = \sum_i A_i \exp(-t/\tau_i) \tag{1}$$

Here, A_i are unknown amplitudes determined via least-squares fitting, and τ_i are assumed time constants spanning the time-delay range sampled by the EM system (from the earliest off-time channel at 88.781 μs to the latest at 2,936.004 μs, with 17 channels in total). The exponential functions are convolved with the system waveform and fitted to the observed data to obtain the A_i values. This step compresses the data into a waveform-independent representation in tau space.

b) Estimation of Mirror-Image Depths: Assuming the inductive limit, the secondary magnetic field is modeled as a mirror image of the transmitter loop [15]. The mirror image starts at a depth equal to the transmitter height (nominal 30 m) below the ground surface and recedes with increasing time. The mirror-depth h_i beneath the receiver at time t_i is estimated using an iterative scheme supported by a precomputed lookup table that accounts for the logarithm of the field and its derivative with respect to log depth.

c) Computation of Cumulative Conductance: Conductivity is derived from the second derivative of time delay with respect to depth [33]:

$$\sigma_i = \frac{1}{\mu_0}\frac{\partial^2 t}{\partial h^2} \tag{2}$$

To avoid numerical instabilities from the second derivative, the equation is integrated to obtain cumulative conductance as a function of depth [34]. The derivative ∂t/∂h is estimated using the chain rule:

$$\frac{\partial t}{\partial h} = \frac{\partial t}{\partial A}\frac{\partial A}{\partial h} \tag{3}$$

where $\partial t/\partial A$ is obtained from the step-response equation, and $\partial A/\partial h$ is computed numerically [34].

d) Derivation of Apparent Conductivity: Once cumulative conductance is obtained, apparent conductivity is derived by first dividing the estimated penetration depth (up to ~300 m) into a limited number of coarse depth segments (typically 10–20). This coarse segmentation is used internally to stabilize the piecewise linear fitting and is independent of the final vertical discretization used for the CDI output. This method ensures stability and allows flexibility for variable layer thicknesses while mitigating noise sensitivity compared to direct differentiation.

e) Parameterization and Damped Inversion: To derive the final conductivity-depth section, the conductivity function is parameterized using cubic polynomials on depth intervals defined by penetration depths. Conductivity in each interval is defined by values and first derivatives at bounding nodes to maintain continuity. This leads to an underdetermined linear system, solved via damped matrix inversion to minimize squared residuals between observed and predicted data. Smoothness constraints are applied: first-derivative damping for flat profiles and second-derivative damping for smoother variations. Resistivity weighting scales the smoothness matrices by average interval conductivity to suppress artifacts in resistive zones [15].

f) Generation of CDI Sections and Pseudo-3D Model: Independent CDI sections are generated for each flight line. These 2D sections are then interpolated using multidimensional linear interpolation to form a quasi-3D conductivity model, accounting for the 200 m line spacing and incorporating local topography.

This workflow provides a rapid, stable approximation of subsurface conductivity, suitable for initial imaging before full quantitative inversion.

Table 1. Electrical resistivity values of the rock samples collected from the Granisle deposit [32].

Rock Type	Alteration	Resistivity (Ωm)
Biotite-feldspar porphyry	Phyllic	761
		200
	Potassic	3472
		2223
		1823
		5948
		1436
	Weak potassic	9942
Biotite-feldspar porphyry dike	Potassic	1928
Quartz-diorite microporphyry	Qtz-ser-carb-py	-
		-
	Potassic	5258
		4896
Andesitic tuff	Phyllic	560
		2073
		-
		-
Extrusive equiv of BFP	Weak carb-bt	65
	Least-altered	96
Granite	Least-altered	4412
		1244

4. Results and discussion

The interpretation of AeroTEM airborne time-domain electromagnetic data over the Granisle deposit was structured in four sequential stages, progressing from initial data evaluation to practical applications. First, qualitative analysis of off-time channels and the Late Time Decay Constant (τ) map was conducted to delineate major conductivity anomalies. Second, conductivity-depth imaging (CDI) was applied line-by-line, with sections interpolated to form a pseudo-3D conductivity model that captures the anomaly's geometry and depth extent. Third, these conductivity patterns were correlated with known evolution of the EM response. Fourth, the implications for exploration targeting and mining engineering were evaluated, emphasizing CDI's role in reducing subsurface uncertainty and guiding future investigations.

4.1. Qualitative analysis of off-time channel responses and τ map

Analysis of spatial and temporal variations in off-time channel amplitudes enables rapid identification of major conductive trends and potential targets prior to CDI (Figure 4). In each time channel, higher

Table 2. Key parameters used in the CDI algorithm.

Parameter	Value/Setting	Description
Input data format	line number; fiducial; X, Y, Z coordinates; altitude; Z (ASL = topography + altitude); 17 off-time channels	Station positions, elevation data (for depth referencing), and raw TEM responses used for georeferenced CDI sections.
Number of off-time channels	17	Off-time channels from AeroTEM III data, used for transformation to step-response waveform.
Delay time range (time constants, τ_i)	88.781 µs to 2,936.004 µs	Range spanning the sampled off-time channels; logarithmically spaced for tau-space representation.
System waveform	Triangular pulse at 90 Hz	Excitation waveform convolved during transformation to step-response.
Nominal sensor altitude	30 m	Average flight height used in mirror-image depth estimation; incorporates topography variations from input Z (ASL).
Line spacing	200 m	Survey line spacing, influencing interpolation for pseudo-3D model.
Number of tau (basis functions)	34	User-specified number of time constants for deconvolution; typically 1.5-2 times the number of channels for time-domain data to fit complex decays
Smoothing factor	0.5	Weight in deconvolution favoring smooth amplitude solutions in tau-domain; minimizes errors and striping in CDI (user-selected for study data).
Depth resolution	1 m	Vertical step size for conductivity calculations; determines effective number of depth intervals (user-selected for smooth imaging).
Number of depth intervals	Approximately 300 (up to ~300 m penetration)	Derived from effective depth of investigation / vertical resolution; number of output depth samples used for CDI visualization.
Resistivity weighting	Enabled (scaled by average interval conductivity)	Applied to smoothness matrices to suppress artifacts in high-resistivity zones.
Interpolation method	Multidimensional linear	Used to merge 2D CDI sections into quasi-3D model, accounting for line spacing and topography (post-processing).

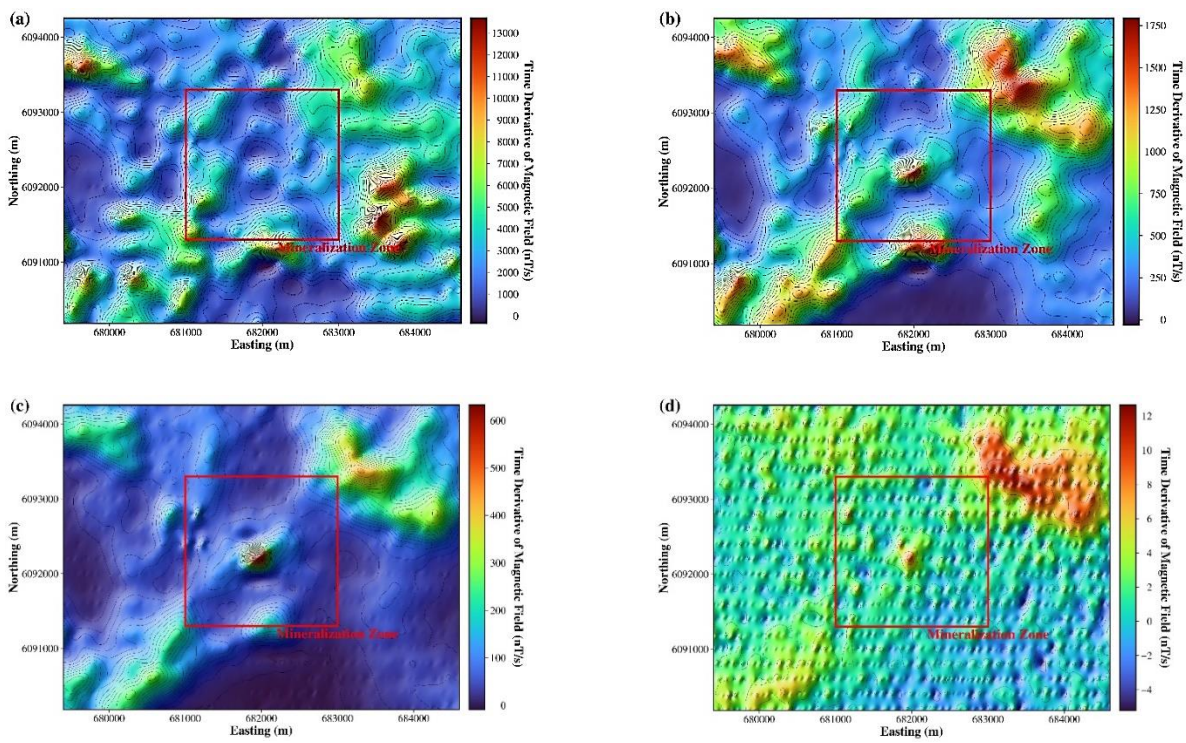

Figure 4. Four representative channels from the 17 off-time channels of the airborne EM dataset over the study area: (a) off-time channel 0 (88.781 µs after current shutoff), (b) off-time channel 5 (227.670 µs), (c) off-time channel 10 (644.337 µs), and (d) off-time channel 16 (2,936.004 µs). These panels illustrate the temporal

positive amplitudes indicate zones of more conductive materials within the subsurface volume governing the response at that delay time. In Channel 0 (88.781 µs after current shutoff), the Granisle deposit exhibits only a weak response, partly masked by highly resistive material.

By Channel 5 (227.670 µs), a pronounced anomaly emerges, forming a strong, focused conductive core with sharp boundaries that stands out clearly from the resistive surroundings. This concentration in mid-delay channels reflects optimal coupling between the induced field and a strong conductor at moderate depths. In Channel 10 (644.337 µs), the anomaly weakens slightly but remains distinct, with a more evident northeast–southwest elongation previously seen in Channel 5—behavior consistent with the diffusion of induced currents and the geometry of an ore-bearing body. In the final channel (2,936.004 µs), data become considerably noisier and the magnetic-field amplitude diminishes significantly; nevertheless, the anomaly remains partially visible, displaying a more diffuse pattern typical of late-time channels influenced by current diffusion around a confined conductor at shallow to moderate depths.

This temporal progression—from initial masking by highly resistive materials, to concentration and peak intensity at mid-delay times, followed by gradual expansion and decay at late times—is characteristic of a highly conductive sulfide source located at moderate to relatively

significant depths. Assuming a conductivity of approximately 25 mS/m and using diffusion-based approximations, the strong, localized signatures observed in Channels 5–10 indicate that the top of the conductor lies at roughly 60–100 m depth. Moreover, persistence of the anomaly in late-time channels suggests a substantial vertical extent, likely exceeding 200 m. The northeast–southwest elongation visible in mid-delay channels likely reflects structural controls or the orientation of shear zones and vein networks.

The Late Time Decay Constant (τ) provides a stable, direct, quasi-quantitative indicator of subsurface conductivity because it is directly linked to the decay rate of the secondary field; conductive regions exhibit larger τ values due to prolonged induced-current lifetimes. The τ map (Figure 5) reveals three principal conductive zones across the area, collectively defining a southwest–northeast-trending conductive system consistent with temporal-channel responses. The northeastern zone, characterized by moderately high τ values, likely corresponds to porous Jurassic sedimentary rocks (Smithers and Ashman Groups), while the southwestern zone with mildly elevated τ corresponds to Eocene breccias. The most prominent zone lies centrally, coincident with the Granisle deposit, and stands out distinctly from the surrounding resistive background. Its uniformly elevated τ indicates not only strong signal amplitude but also slow decay, typical of highly conductive sulfide-bearing rocks. The spatial coherence, consistent width, and uniform strike of this feature signify a focused conductive structure with a deep-rooted origin. In contrast, areas with lower τ surrounding this body represent resistive units lacking significant mineralization and exhibiting rapid decay.

Collectively, off-time channels and the τ map delineate the surface expression of a vertically persistent, highly conductive zone. The mid-delay anomalies, sharp boundaries, strong magnetic-field gradients, and consistent τ pattern define a high-priority drill target and the most probable locus of alteration and mineralization.

4.2. Conductivity-depth maging and the pseudo-3D conductivity model

Building on qualitative insights from off-time channels and τ patterns, CDI was performed independently for each flight line, generating a series of quasi-2D sections (Figure 6a). Consistent with expectations from τ analysis and mid-delay behavior, results reveal a distinct conductive core in the central survey area at relatively shallow depth, directly beneath the current mining pit. This conductive concentration appears consistently along adjacent lines, demonstrating spatial reproducibility and reducing the likelihood of orientation-related artifacts or limitations inherent in 1D imaging.

Given the nominal 200 m line spacing and data gaps between lines, a multidimensional linear interpolation method was applied to construct a pseudo-3D conductivity model (Figure 6b). Although CDI inherently produces vertically smeared responses owing to its 1D formulation, the structural coherence of the interpolated model with trends observed on adjacent lines indicates that it still provides a meaningful and continuous image of the subsurface conductive core.

To more precisely assess the three-dimensional geometry of the conductive body and to constrain its vertical and lateral extent, two orthogonal vertical sections (north–south and east–west), together with a horizontal slice at an elevation of approximately 570 m, were extracted (Figure 7). These sections delineate a focused conductive core characterized by relatively high conductivity values which is consistently developed within an elevation range of approximately 500 to 600 m. In addition, weaker conductive responses with limited continuity can be traced to lower elevations, down to approximately 450 m. The correspondence between this vertical distribution, the persistence of late-time electromagnetic responses, and the gradual increase in τ indicates that the conductive core represents a genuine geological unit or a sulfide-bearing mineralized zone, rather than an artifact related to surface effects or inherent limitations of the one-dimensional CDI approach.

To evaluate the reliability of depth-related interpretations, the depth sensitivity of the time-domain electromagnetic method was examined. Based on half-space approximations and signal decay characteristics, early-time channels primarily resolve shallow structures, whereas later-time channels respond to progressively deeper features. However, the overall depth of investigation is controlled by the signal-to-noise ratio and the background resistivity. For the Granisle dataset, assuming a sensor altitude of approximately 30 m and moderate background resistivity values derived from rock property measurements [32], the effective depth of investigation is estimated to be on the order of 250–300 m, consistent with AeroTEM [35] and similar time-domain airborne EM applications [36] in overburden-covered terrains in British Columbia. Despite this, the conductive anomaly is mainly concentrated at shallower levels, and at greater depths the model becomes progressively less constrained by the data and increasingly influenced by transformation assumptions. These limitations define the vertical interval over which conductivity anomalies can be interpreted with greater confidence, thereby focusing the interpretation on the upper ~250 m of the vertical section where the strongest correspondence with geological zoning is observed.

4.3. Geological interpretation conductivity

To establish a conceptual geological framework, conductivity sections extracted from the CDI model (Figure 7) were used as the primary basis for interpretation. In the absence of direct subsurface data such as drilling information, the discrimination of alteration zones was carried out based on the conductivity patterns of the CDI model and geological descriptions from previous studies. Accordingly, the potassic, phyllic, and propylitic alteration zones that are typically developed in Babine-type porphyry deposits, including Granisle, were considered [28]. For example, Dirom et al. (1995) describe the Granisle deposit as exhibiting a well-developed biotite–magnetite (potassic) and propylitic alteration assemblage whereas the quartz–sericite–pyrite (phyllic) alteration forms a more restricted zone. The principal sulfide minerals include chalcopyrite, bornite, and pyrite, occurring disseminated and within quartz stockworks, and they play a critical role in controlling the electrical properties of the system [28]. Physical property measurements of Granisle rock samples further indicate variations in resistivity that are consistent with alteration type, thereby strengthening the link between CDI anomalies and geological features [32].

The potassic alteration zone, characterized by secondary biotite, magnetite, and K-feldspar, is generally associated with moderate to low conductivity. This response reflects the relative scarcity of highly conductive sulfides and the resistive nature of magnetite-rich assemblages, as supported by physical property studies of Babine porphyry systems [32]. Although this zone is not distinctly resolved in the CDI sections—likely due to its deeper position within the root zone of the system [28]—it is inferred, based on reported zoning patterns, to underlie the main conductive anomaly. To better delineate this magnetite-rich zone, detailed processing and integrated interpretation of the existing airborne magnetic data are recommended, as magnetic methods are highly sensitive to variations in magnetite content and can effectively highlight zones of elevated magnetic susceptibility [37].

The phyllic alteration zone, dominated by sericite, quartz, and pyrite, exhibits high conductivity owing to the presence of disseminated sulfides and clay minerals that enhance ionic conduction [32]. In the CDI sections, this zone corresponds to a prominent high-conductivity core, with conductivity values significantly exceeding background levels and forming an extensive vertical body. This pattern is consistent with the pyrite-rich quartz–sericite alteration at Granisle which is associated with chalcopyrite and bornite mineralization [28]. Physical property measurements of Granisle rock samples indicate that phyllic-altered rocks display substantially higher conductivity than their potassic counterparts, confirming the strong correlation between the CDI anomaly and this alteration type [32]. The spatial coincidence of this anomaly with the historical open pit further supports its association with mapped phyllic alteration zones.

The propylitic alteration zone, comprising chlorite, epidote, and carbonate, forms the outer halo of the system and exhibits intermediate conductivity as a result of variable sulfide content and fluid-related

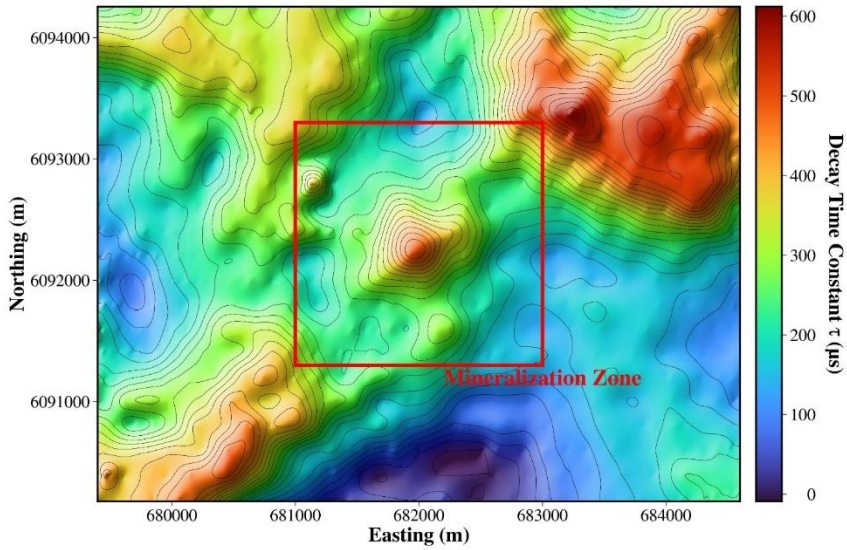

Figure 5. Late time Decay constant (τ) map of the study area. The mineralized zone associated with the Granisle deposit is outlined by a red box. This area was selected to focus subsequent processing steps and to minimize the influence of unrelated anomalies.

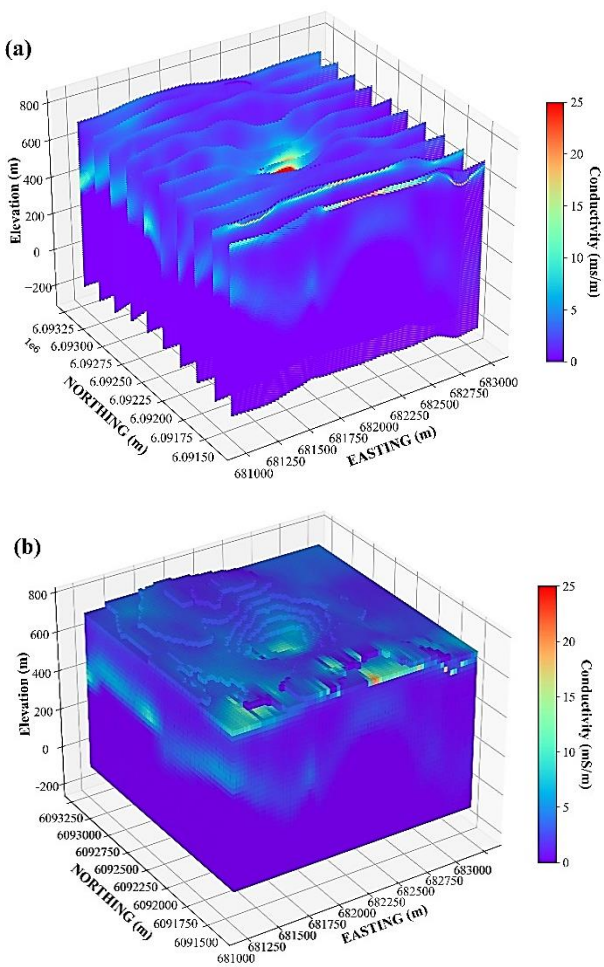

Figure 6. Conductivity-depth imaging (CDI) results generated for each survey line in the study area: (a) three-dimensional view of the ten 2-D pseudo-sections extracted from the flight lines crossing the deposit, and (b) the quasi-3-D model obtained by interpolating these 2-D pseudo-sections, delineating the subsurface conductivity structure of the area.

alteration effects [28, 32]. In the CDI model, this zone corresponds to transitional areas of moderate conductivity that envelop the highly conductive core. These features are less sharply resolved in the model, likely reflecting the subtle conductivity contrasts characteristic of propylitic alteration; nevertheless, they are consistent with the overall zoning patterns reported for Granisle where propylitic assemblages extend outward from the mineralized intrusive rocks.

In evaluating alternative potential sources for the observed conductivity anomaly, such as alteration clays or groundwater, it is noted that phyllic alteration inherently includes sericite (a clay mineral) which contributes to enhanced conductivity through increased porosity and ionic conduction pathways [32]. In addition, the flooded historical open pit at Granisle may promote the accumulation of clays or saline groundwater, potentially elevating near-surface conductivity while Babine Lake may also influence the signal through conductive sediments or water saturation. However, attributing the anomaly to sulfide mineralization is more consistent with the geological context, as the focused geometry of the anomaly and its vertical extent (exceeding 250 m) closely align with the mapped distribution of pyrite-rich phyllic zones and sulfide stockworks in the core of the deposit [28], rather than with the laterally extensive, shallow features typically associated with groundwater. Physical property data from Granisle samples further demonstrate that sulfide-bearing phyllic-altered rocks have significantly lower resistivity than unaltered or potassic-altered rocks, supporting the interpretation that sulfides are the dominant contributors to the observed conductivity anomaly [32].

4.4. Implications for exploration and mining engineering

The quasi-3D conductivity model derived from conductivity–depth imaging (CDI) of the AeroTEM III data provides a first-order interpretive framework for assessing the spatial distribution of conductive zones at the Granisle deposit, rather than a definitive quantitative subsurface model. In this context, the principal value of the results lies in supporting exploration-stage decision-making and in improving the focus of subsequent investigations, particularly in areas where subsurface information is limited.

From an exploration perspective, the CDI results facilitate identification and tracking of the lateral and vertical continuity of conductive zones associated with sulfide mineralization beneath the historical open pit. These insights can assist in prioritizing drill targets, especially in parts of the deposit where surface exposure is poor or structural complexity hampers conventional geological interpretation. It

should be emphasized, however, that CDI alone cannot replace drilling or full three-dimensional inversion; instead, it serves as a complementary tool for constraining the range of plausible subsurface geometries and guiding the design of follow-up exploration programs.

From a mining engineering standpoint, the generalized conductivity patterns provide contextual information on the distribution and continuity of altered and mineralized zones relative to existing and potential extraction areas. Although detailed delineation of ore boundaries, slope stability, and geotechnical conditions requires higher-resolution geological and geophysical data, the CDI-based model can contribute to preliminary assessments of rock-mass behavior and to the planning of targeted geotechnical or geophysical studies.

Overall, the application of time-domain airborne electromagnetic data combined with CDI at Granisle yields a coherent first-order image of subsurface conductivity that supports integration between geophysical observations and geological understanding. The primary contribution of this approach lies in reducing interpretive uncertainty and in providing a rational basis for designing subsequent drilling campaigns or more advanced quantitative inversions within the Granisle deposit.

5. Conclusions

In this study, qualitative interpretation of off-time channels and the Late Time Decay Constant (τ) was integrated with conductivity–depth imaging (CDI) to rapidly and coherently reconstruct the subsurface conductivity architecture of the Granisle porphyry Cu–Au deposit. The results demonstrate that the combined analysis of the temporal behavior of electromagnetic responses and the quasi-3D CDI model effectively resolves the principal conductive zones, their lateral geometry, and their vertical continuity with a reasonable level of confidence. The CDI results delineate a focused conductive core beneath the historical open pit, developed predominantly within an elevation range of approximately 500–600 m above sea level. The geometry and spatial position of this zone show strong consistency with the established alteration framework, the distribution of sulfide mineralization, and available rock physical property data. The spatial coherence of anomalies across mid- and late-time channels, together with the stability of the τ pattern and the persistence of responses in depth sections, collectively indicate that the identified anomalies reflect genuine geological structures rather than processing artifacts.

Accordingly, this integrated approach provides a geologically robust first-order image of subsurface conductivity at Granisle, which can serve as a reliable foundation for structural interpretation, drill-target prioritization, and the design of subsequent quantitative inversion stages within the Granisle deposit. Although the resolution of CDI is more limited compared to full three-dimensional inversion, its high processing speed, computational efficiency, and effectiveness in exploration targeting render it a valuable tool for the early stages of mineral exploration. However, as CDI constitutes a rapid one-dimensional approximation based on a pseudolayer half-space model and point-by-point processing of airborne electromagnetic (AEM) data, it inherently possesses certain limitations. Among these is vertical smearing whereby noise in low-amplitude responses—particularly in noisy datasets—can manifest as artificial banding or spurious conductivity at depth. This effect can be partially mitigated by incorporating on-time data and broadening the system's response bandwidth. Furthermore, in complex three-dimensional geological settings—such as areas with faults or sharp lateral discontinuities—the one-dimensional layered earth assumption may lead to averaging of responses over the system footprint, resulting in distortion of the outcomes. Such distortions can cause blurring of true boundaries, incorrect positioning of conductive zones, or misinterpretation of structural dips; for instance, unresolved thin resistive intrusions may mask responses from deeper units. Consequently, while CDI performs admirably in terrains with relatively horizontal layering or extensive regolith for rapid background mapping, in heterogeneous environments it should be supplemented with targeted three-dimensional modeling or multi-line validation to enhance the accuracy of geological interpretations.

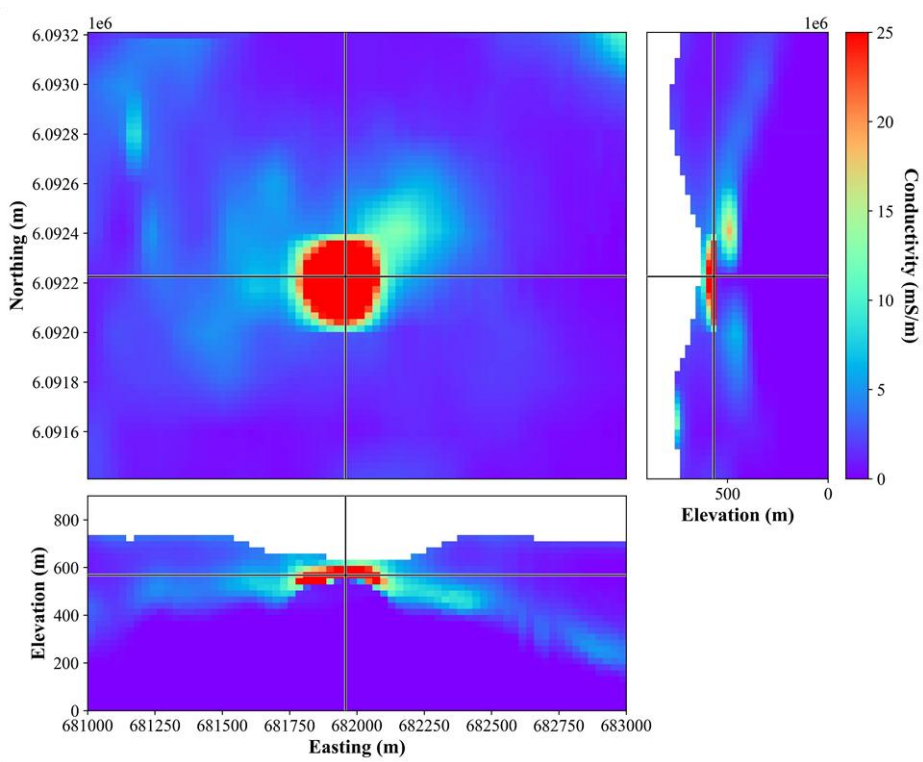

Figure 7. Three selected sections extracted from the quasi-3-D conductivity model: two vertical sections and one horizontal section, providing a detailed view of the subsurface structure and conductivity distribution within the study area.

Overall, the findings of this study highlight the broader applicability of a time-domain airborne electromagnetic (AEM) workflow integrated with conductivity-depth imaging (CDI) as an effective reconnaissance-to-targeting tool in porphyry exploration. By delivering rapid, geologically coherent first-order conductivity models without the computational burden of full inversion, this approach offers a practical means of reducing exploration uncertainty and guiding decision-making in covered or structurally complex terrains. In porphyry Cu–Au systems comparable to Granisle, where conductive alteration and sulfide distributions exert strong control on geophysical responses, such a methodology can significantly enhance early-stage target prioritization and provide a robust foundation for subsequent detailed modeling and drilling programs.

References

[1]. Yin, C. C., Zhang, B., Liu, Y. H., Ren, X. Y., Qi, Y. F., Pei, Y. F., et al. (2015). Review on airborne EM technology and developments. *Acta Geophysica Sinica*, 58(8), 2637–2653. doi: http://dx.doi.org/10.6038/cjg20150804

[2]. Yang, D., & Oldenburg, D. W. (2012). Three-dimensional inversion of airborne time-domain electromagnetic data with applications to a porphyry deposit. *Geophysics*, 77(1), B23–B34. doi: http://dx.doi.org/10.1190/geo2011-0194.1

[3]. Abraham, J., Minsley, B., Bedrosian, P., Smith, B., & Cannia, J. (2012). Airborne electromagnetic surveys for groundwater characterization. *ASEG Extended Abstracts*, 2012, 1–1. doi: http://dx.doi.org/10.1071/ASEG2012ab246

[4]. Harrison, E. J., Baranwal, V. C., Pfaffhuber, A. A., Christensen, C. W., Skurdal, G. H., Rønning, J. S., et al. (2021). AEM in Norway: A review of the coverage, applications and the state of technology. *Remote Sensing*, 13(23), 4687. doi: http://dx.doi.org/10.3390/rs13234687

[5]. Auken, E., Boesen, T., & Christiansen, A. V. (2017). A review of airborne electromagnetic methods with focus on geotechnical and hydrological applications from 2007 to 2017. In L. B. Nielsen (Ed.), *Advances in Geophysics* (pp. 47–93). Elsevier. doi: http://dx.doi.org/10.1016/bs.agph.2017.10.002

[6]. Siemon, B., Christiansen, A., & Auken, E. (2009). A review of helicopter-borne electromagnetic methods for groundwater exploration. *Near Surface Geophysics*, 7(6), 629–646. doi: http://dx.doi.org/10.3997/1873-0604.2009052

[7]. Ranjbar, H., Hassanzadeh, H., Torabi, M., & Ilaghi, O. (2001). Integration and analysis of airborne geophysical data of the Darrehzar area, Kerman Province, Iran, using principal component analysis. *Journal of Applied Geophysics*, 48, 33–41. doi: http://dx.doi.org/10.1016/S0926-9851(01)00059-3

[8]. Shirzaditabar, F., Bastani, M., & Oskooi, B. (2011). Imaging a 3D geological structure from HEM, airborne magnetic and ground ERT data in the Kalat-e-Reshm area, Iran. *Journal of Applied Geophysics*, 75, 513–522. doi: http://dx.doi.org/10.1016/j.jappgeo.2011.08.006

[9]. Abedi, M., Fournier, D., Devriese, S. G. R., & Oldenburg, D. W. (2018). Integrated inversion of airborne geophysics over a structural geological unit: A case study for delineation of a porphyry copper zone in Iran. *Journal of Applied Geophysics*, 152, 188–202. doi: http://dx.doi.org/10.1016/j.jappgeo.2018.04.001

[10]. Ghari, H. A., Voge, M., Bastani, M., Pfaffhuber, A. A., & Oskooi, B. (2020). Comparing resistivity models from 2D and 1D inversion of frequency-domain HEM data over rough terrains: Case studies from Iran and *Norway. Exploration Geophysics, 51, 45–65. doi: http://dx.doi.org/10.1080/08123985.2019.1588068*

[11]. Dentith, M., & Mudge, S. T. (2014). *Geophysics for the Mineral Exploration Geoscientist*. Cambridge University Press. doi: http://dx.doi.org/10.1017/CBO9781139024358

[12]. Pearce, C. I., Pattrick, R. A. D., & Vaughan, D. J. (2006). Electrical and magnetic properties of sulfides. *Reviews in Mineralogy and Geochemistry*, 61(1), 127–180. doi: http://dx.doi.org/10.2138/rmg.2006.61.3

[13]. Guo, Z., Xue, G., Liu, J., & Wu, X. (2020). Electromagnetic methods for mineral exploration in China: A review. *Ore Geology Reviews*, 118, 103357. doi: http://dx.doi.org/10.1016/j.oregeorev.2020.103357

[14]. Lu, C., Wang, J., & Huang, S. (2025). An iterative laterally constrained inversion scheme for time-domain airborne electromagnetic data. *Journal of Applied Geophysics*, 238, 105729. doi: http://dx.doi.org/10.1016/j.jappgeo.2025.105729

[15]. Macnae, J. C., Smith, R., Polzer, B. D., Lamontagne, Y., & Klinkert, P. S. (1991). Conductivity-depth imaging of airborne electromagnetic step-response data. *Geophysics*, 56(1), 102–114. doi: http://dx.doi.org/10.1190/1.1442945

[16]. Yin, C., Ren, X., Liu, Y., Qi, Y., Qiao, C., & Jing, C. (2015). Review on airborne electromagnetic inverse theory and applications. *Geophysics*, 80(4), W17–W31. doi: http://dx.doi.org/10.1190/geo2014-0544.1

[17]. Macnae, J., King, A., Stolz, N., Osmakoff, A., & Blaha, A. (1998). Fast AEM data processing and inversion. *Exploration Geophysics*, 29(1–2), 163–169. doi: http://dx.doi.org/10.1071/EG998163

[18]. Huang, H., & Rudd, J. (2008). Conductivity-depth imaging of helicopter-borne TEM data based on a pseudolayer half-space model. *Geophysics*, 73(4), F115–F120. doi: http://dx.doi.org/10.1190/1.2904984

[19]. Liang, S., Sun, S., & Lu, H. (2021). Application of airborne electromagnetics and magnetics for mineral exploration in the Baishiquan–Hongliujing area, northwest China. *Remote Sensing*, 13(5), 903. doi: http://dx.doi.org/10.3390/rs13050903

[20]. Stolz, R., Schiffler, M., Becken, M., Thiede, A., Schneider, M., Chubak, G., et al. (2022). SQUIDs for magnetic and electromagnetic methods in mineral exploration. *Mineral Economics*, 35(4), 467–494. doi: http://dx.doi.org/10.1007/s13563-022-00333-3

[21]. Sinclair, W. (2007). Porphyry deposits. In W. D. Goodfellow (Ed.), *Mineral Deposits of Canada* (pp. 223–243). Geological Association of Canada.

[22]. Sillitoe, R. H. (2010). Porphyry copper systems. *Economic Geology*, 105(1), 3–41. doi: http://dx.doi.org/10.2113/gsecongeo.105.1.3

[23]. Lowell, J. D., & Guilbert, J. M. (1970). Lateral and vertical alteration–mineralization zoning in porphyry ore deposits. *Economic Geology*, 65(4), 373–408. doi: http://dx.doi.org/10.2113/gsecongeo.65.4.373

[24]. Beane, R. E., & Bodnar, R. J. (1995). Hydrothermal fluids and hydrothermal alterations in porphyry copper deposits. In F. W. Pierce & J. G. Bohm (Eds.), *Porphyry Copper Deposits of the American Cordillera* (pp. 83–93). Arizona Geological Society.

[25]. Oldenburg, D. W., Li, Y., & Ellis, R. G. (1997). Inversion of geophysical data over a copper–gold porphyry deposit: A case history for Mt. Milligan. *Geophysics*, 62(5), 1419–1431. doi: http://dx.doi.org/10.1190/1.1444246

[26]. Wallace, W. S. (1935). *The Encyclopedia of Canada*. University Associates of Canada.

[27]. John, D. A., Ayuso, R. A., Barton, M. D., Blakely, R. J., Bodnar, R. J., Dilles, J. H., et al. (2010). Porphyry copper deposit model. In *Mineral Deposit Models for Resource Assessment* (U.S. Geological Survey Scientific Investigations Report 2010-5070-B). doi: http://dx.doi.org/10.3133/sir20105070B

[28]. Dirom, G. E., Dittrick, M. P., McArthur, D. R., Ogryzlo, P. L., Pardoe, A. J., & Stothart, P. G. (1995). Bell and Granisle porphyry copper–gold mines, Babine region, west-central British Columbia. In T. G. Schroeter (Ed.), *Porphyry Deposits of the Northwestern Cordillera of North America* (pp. 255–288). Canadian Institute of Mining, Metallurgy and Petroleum.

[29]. Walker, S., & Garrie, D. (2009). *Report on a Helicopter-Borne AeroTEM System Electromagnetic & Magnetic Survey*. Aeroquest Limited.

[30]. MacIntyre, D. G., & Villeneuve, M. E. (2001). Geochronology of mid-Cretaceous to Eocene magmatism, Babine porphyry copper district, central British Columbia. *Canadian Journal of Earth Sciences*, 38(4), 639–655. doi: http://dx.doi.org/10.1139/e00-107

[31]. MacIntyre, D. G., Villeneuve, M. E., & Schiarizza, P. (2001). Timing and tectonic setting of Stikine Terrane magmatism, Babine–Takla lakes area, central British Columbia. *Canadian Journal of Earth Sciences*, 38(3), 579–601. doi: http://dx.doi.org/10.1139/e00-105

[32]. Mitchinson, D., Enkin, R., & Hart, C. (2013). Linking porphyry deposit geology to geophysics via physical properties: Adding value to Geoscience BC geophysical data *(Geoscience BC Report 2013-14)*. Retrieved from https://www.geosciencebc.com/projects/2009-001/

.[33]. Macnae, J., & Lamontagne, Y. (1987). Imaging quasi-layered conductive structures by simple processing of transient electromagnetic data. *Geophysics*, 52(5), 545–554. doi: http://dx.doi.org/10.1190/1.1442323

[34]. Macnae, J. (2004). Improving the accuracy of shallow depth determinations in AEM sounding. *Exploration Geophysics*, 35(2), 203–207. doi: http://dx.doi.org/10.1071/EG04203

[35]. Caron, R. M., Samson, C., Bates, M., & Chouteau, M. (2018). Correcting airborne gravity data for overburden thickness: A case study from the Nechako Interior Plateau, British Columbia. *Canadian Journal of Earth Sciences*, 56, 483–492. doi: http://dx.doi.org/10.1139/cjes-2017-0209

[36]. Mitchinson, D., Fournier, D., Hart, C., Astic, T., & Chouteau, M. (2022). Identification of new porphyry potential under cover in British Columbia. (*Geoscience BC Report 2022-07)*. Retrieved from https://www.geosciencebc.com/projects/2022-002/

[37]. Mostafaei, K., & Kianpour, M. (2022). Application of magnetometry in Manto-type copper deposit exploration: Case study of the Meyami area, Iran. *Rudarsko-Geološko-Naftni Zbornik*, 37. doi: http://dx.doi.org/10.17794/rgn.2022.5.1

[38]. Cui, Y., Miller, D., Schiarizza, P., & Diakow, L. J. (2017). *British Columbia Digital Geology* (British Columbia Geological Survey Open File 2017-8). British Columbia Ministry of Energy, Mines and Petroleum Resources.